WARWICK
THE UNIVERSITY OF WARWICK

Manuscript version: Author's Accepted Manuscript
The version presented in WRAP is the author's accepted manuscript and may differ from the published version or Version of Record.

Persistent WRAP URL:
http://wrap.warwick.ac.uk/114963

How to cite:
Please refer to published version for the most recent bibliographic citation information. If a published version is known of, the repository item page linked to above, will contain details on accessing it.

Copyright and reuse:
The Warwick Research Archive Portal (WRAP) makes this work by researchers of the University of Warwick available open access under the following conditions.

© 2019 Elsevier. Licensed under the Creative Commons Attribution-NonCommercial-NoDerivatives 4.0 International http://creativecommons.org/licenses/by-nc-nd/4.0/.

Publisher's statement:
Please refer to the repository item page, publisher's statement section, for further information.

For more information, please contact the WRAP Team at: wrap@warwick.ac.uk.

warwick.ac.uk/lib-publications

Accepted Manuscript

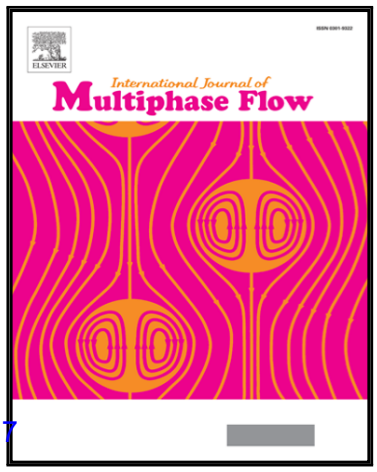

Investigating the jamming of particles in a three-dimensional fluid-driven flow via coupled CFD–DEM simulations

Honglei Sun, Shanlin Xu, Xiaodong Pan, Li Shi, Xueyu Geng, Yuanqiang Cai

PII: S0301-9322(18)30528-7
DOI: https://doi.org/10.1016/j.ijmultiphaseflow.2019.01.017
Reference: IJMF 2974

To appear in: *International Journal of Multiphase Flow*

Received date: 21 July 2018
Revised date: 6 January 2019
Accepted date: 17 January 2019

Please cite this article as: Honglei Sun, Shanlin Xu, Xiaodong Pan, Li Shi, Xueyu Geng, Yuanqiang Cai, Investigating the jamming of particles in a three-dimensional fluid-driven flow via coupled CFD–DEM simulations, *International Journal of Multiphase Flow* (2019), doi: https://doi.org/10.1016/j.ijmultiphaseflow.2019.01.017

This is a PDF file of an unedited manuscript that has been accepted for publication. As a service to our customers we are providing this early version of the manuscript. The manuscript will undergo copyediting, typesetting, and review of the resulting proof before it is published in its final form. Please note that during the production process errors may be discovered which could affect the content, and all legal disclaimers that apply to the journal pertain.

ACCEPTED MANUSCRIPT

Highlights

- Compared with previous works that studied the effect of concentration and size ratio on jamming separately, we combine the effect of ϕ_0 and R on the jamming probability P_{jam}. We plot the jamming probability on the ϕ_0-R plane and match the different ranges of ϕ_0 and R to three different jamming states. Accordingly, we explain the coupled effect of ϕ_0 and R on jamming from the view of the maximum particle discharge capacity of the orifice.
- Another quantity of interest that we studied is the complex influence of the fluid velocity U_f on jamming. It is found that the influence of the fluid velocity on jamming differs in different range of solid concentration, e.g., the "sequential bridging" jamming only occurs in low-speed and low-solid concentration flow. Moreover, for the "multi-particle" fluid-driven jamming, the jamming probability increases with the fluid velocity because the particle discharge rate increases with the fluid velocity. However, it is noted that when the fluid velocity U_f is high, U_f has little effect on the particle discharge rate and therefore the insignificant influence on the jamming probability.
- We also investigate the particle discharge properties and relate the particle discharge rate to the occurrence of jamming under different conditions. It is found that for a given size ratio R, the orifice has a maximum discharge capacity, and once the particle discharge rate reaches to the maximum particle discharge capacity of orifice, jamming is possible to happen.
- Because of the ability of the coupled CFD–DEM method to calculate the particle motion and contact force, the shape of the three-dimensional particle jamming dome and the force chain of clogged particles are investigated. For the first time, we find that the jamming arch that is formed under a higher flow velocity has a larger curvature due to the greater fluid drag acted on the jammed particles.

ACCEPTED MANUSCRIPT

ACCEPTED MANUSCRIPT

Investigating the jamming of particles in a three-dimensional fluid-driven flow via coupled CFD–DEM simulations

Honglei Sun[a], Shanlin Xu[b], Xiaodong Pan[c,*], Li Shi[c], Xueyu Geng[d], Yuanqiang Cai[b]

[a]*Institute of Disaster Prevention and Reduction Engineering and Protective Engineering, College of Civil Engineering and Architecture, Zhejiang University, Hangzhou 310027, PR China*
[b]*Research Center of Coastal and Urban Geotechnical Engineering, College of Civil Engineering and Architecture, Zhejiang University, Hangzhou, PR China*
[c]*Institute of Geotechnical Engineering, College of Civil Engineering and Architecture, Zhejiang University of Technology, Hangzhou 31000, PR China*
[d]*School of Engineering, University of Warwick, Coventry, UK*

Abstract

The clogging of a dense stream of particles when passing through an orifice occurs ubiquitously in both natural and industrial fields. Since most of the jamming phenomena lead to the negative effects, studying and preventing jamming is of great importance. There are two typical types of jamming due to different types of driving force: (a) gravity-driven jamming and (b) fluid-driven jamming. Among these two types of jamming, the fluid-driven jamming occurs in fluid-driven particle flows, and the initial solid concentration, the fluid velocity, and the orifice-particle size ratio has been demonstrated to have effects on the occurrence of this jamming. Although the individual influence of the initial solid concentration and orifice-particle size ratio on jamming has been studied, the coupled effects of these two factors on jamming are little known. In addition, the complex effects of the fluid velocity on jamming have not been fully discussed. To address these problems, this work performs a three-dimensional simulation of the fluid-driven jamming using the coupled Computational Fluid Dynamics–Discrete Element Method (CFD–DEM) model. At first, the jamming probability under different initial conditions is studied. The jamming probability is displayed on the solid concentration–orifice size ratio plane to illustrate the coupled effects of these two factors on jamming. The simulation results show that the critical solid concentration, at which the jamming probability increases to 1, increases with the orifice-particle size ratio. This is because an orifice with a larger orifice size ratio has a greater particle discharge capacity, which allows more particles to pass through without jamming. Then, we reveal the influence of fluid velocity over a wide range on the fluid-driven jamming type, jamming probability and shape of the jamming dome. To the author's knowledge, this is the first time that the shape of the jamming dome has

*Corresponding author. Tel: +86 130 6571 0028. Liuhe Road, Xihu District, College of Civil Engineering and Architecture, Zhejiang University of Technology, Hangzhou 31000, PR China

Email addresses: sunhonglei@zju.edu.cn (Honglei Sun), xuxiaoshan7@126.com (Shanlin Xu), panxd@126.com (Xiaodong Pan), lishi@zjut.edu.cn (Li Shi), xueyu.geng@warwick.ac.uk (Xueyu Geng), caiyq@zju.edu.cn (Yuanqiang Cai)

ACCEPTED MANUSCRIPT

been related to the fluid velocity. The jamming dome formed in the higher-speed flow has a greater curvature due to the greater fluid drag acting on the particles.

Keywords: Jamming, CFD–DEM, Fluid-driven particle flow, Multi-particle bridging, Jamming arch, Force chain

1. Introduction

The jamming phenomena of particulate flow systems occur ubiquitously in both natural and industrial processes. When a dense stream of particles competitively flows through an orifice, the solid particles sometimes clog at the orifice and stop flowing. For example, wheat and other grains jam a hopper or silo, preventing the flow (Mondal et al., 2016), powdered raw materials clog conduits and cease their conveyance (Liu and Nagel, 1998), and the clogging occurs in the transport and retention of sand in downhole completions in oil and gas wells (Mondal, 2013). To prevent the jamming phenomena in granular flows, most of which lead to the negative or hazardous effects, considerable research has been conducted on the formation and underlying factors of jamming.

Based on previous works, there are two types of particle jamming from the view of driving force: (a) gravity-driven jamming and (b) fluid-driven jamming. The gravity-driven jamming usually occurs in silos and hoppers under the effect of gravity and has been extensively studied through experimental and numerical methods (To et al., 2001; Zuriguel et al., 2005; Hilton and Cleary, 2011; Janda et al., 2012). The other type of particle jamming, which is called fluid-driven jamming, happens in the fluid-driven granular flows (Guariguata et al., 2012). The particles transported by a fluid flow sometimes clog at the orifice due to the balance of the frictional force and drag force. For both types of jamming, the major contributing factor is the orifice-particle size ratio R, which is defined as a ratio of the orifice size D_o to the particle diameter d_p ($R = D_o/d_p$). With increasing orifice size ratio R, the jamming probability decreases (Zuriguel et al., 2005; Lafond et al., 2013; Mondal et al., 2016).

Although these two types of jamming share some commonalities, they also have their distinct characteristics. Compared with gravity-driven jamming, fluid-driven jamming is influenced by more factors, such as the initial solid concentration ϕ_0 and the fluid velocity U_f. For most of the gravity-driven jamming that occurs in the silo or the hopper, since the particles are initially packed in the silo or hopper, the initial solid concentration ϕ_0 is usually defined as the particle natural packing density (Hilton and Cleary, 2011). The value of ϕ_0 does not vary significantly at different gravity-driven jamming, and Zuriguel et al. (2005) gave ϕ_0 a small range $0.52 \sim 0.64$. However, for fluid-driven jamming, the particles keep buoyant and are entrained by the flows. The initial solid concentration of the fluid-driven flow can vary over a great range. Hence, the study of the influence of the initial solid concentration ϕ_0 on the fluid-driven jamming is of great importance. Mondal et al. (2016) found that the occurrence of the fluid-driven jamming is strongly dependent on ϕ_0. The jamming probability P_{jam} increases with the solid concentration of the particle flow

ACCEPTED MANUSCRIPT

ϕ_0 until ϕ_0 reaches to a critical value $\phi_{critical}$. When $\phi_0 > \phi_{critical}$, the jamming phenomenon definitely occurs ($P_{jam} = 1$). Apart from the initial solid concentration, as the fluid velocity U_f determines the hydrodynamic interaction force between the fluid and particles, the fluid velocity also influences the jamming probability. However, the effect of U_f on jamming is not very clear. From the experiments of Dai and Grace (2010) on the nonspherical particle jamming ($U_f = 0.59 \sim 1.04$ m/s, Re $= 21800 \sim 38100$), Dai and Grace (2010) proposed that the jamming probability increases with the fluid velocity, and this increase is because a higher velocity causes more particles passing through the constriction simultaneously. Mondal et al. (2016) also observed the same influence of the fluid velocity on the jamming of the spherical particles ($U_f = 0.01 \sim 0.1$ m/s, Re $= 15 \sim 150$). However, in the work of Guariguata et al. (2012)($U_f = 0.14 \sim 0.3$ m/s, Re $= 2940 \sim 6300$), it is found that the jamming probability is weekly dependent on the fluid velocity. As the studies on the effect of U_f on jamming are conflicting, the further investigation about the influence of U_f is necessary.

In this work, we aim to systematically study the influences of the above three different underlying factors, ϕ_0, U_f, and R on the fluid-driven jamming, and the coupled Computational Fluid Dynamics and Discrete Element Method (CFD–DEM) is employed to simulate the three-dimensional jamming phenomenon. The DEM part simulates the particle motion by solving Newton's second law, the CFD part solves the fluid motion based on the Navier-Stokes equation, and the coupled CFD–DEM part is utilized to calculate and exchange the fluid–particle interaction force. This method has been widely employed for simulating the fluidization, sediment transport, sand/silt sedimentation, and many other particle flow problems. This method is considered to be advanced because of its superior computational convenience to that of LBM and its greater capability of elaborating the particle motion than TFM (Zhu et al., 2007). Mondal et al. (2016) studied the two-dimensional fluid-driven jamming problem by the coupled CFD–DEM and demonstrated the viability of this method in studying jamming. However, the simulations of three-dimensional fluid-driven jamming are lacking, and the controlling parameters of jamming still need further investigation. Therefore, this work aims to address the shortage of simulations of three-dimensional fluid-driven jamming and improve the understanding of the effect of these controlling factors on the jamming. The novelties of this work are presented below.

1. Compared with previous works that studied the effect of concentration and size ratio on jamming separately, we combine the effect of ϕ_0 and R on the jamming probability P_{jam}. We plot the jamming probability on the ϕ_0-R plane and match the different ranges of ϕ_0 and R to three different jamming states. Accordingly, we explain the coupled effect of ϕ_0 and R on jamming from the view of the maximum particle discharge capacity of the orifice.
2. Another quantity of interest that we studied is the complex influence of the fluid velocity U_f on jamming. It is found that the influence of the fluid velocity on jamming differs in different range of solid concentration, e.g., the "sequential bridging" jamming only occurs in low-speed and low-solid concentration flow. Moreover, for the "multi-particle" fluid-driven jamming,

ACCEPTED MANUSCRIPT

the jamming probability increases with the fluid velocity because the particle discharge rate increases with the fluid velocity. However, it is noted that when the fluid velocity U_f is high, U_f has little effect on the particle discharge rate and therefore the insignificant influence on the jamming probability.

3. We also investigate the particle discharge properties and relate the particle discharge rate to the occurrence of jamming under different conditions. It is found that for a given size ratio R, the orifice has a maximum discharge capacity, and once the particle discharge rate reaches to the maximum particle discharge capacity of orifice, jamming is possible to happen.
4. Because of the ability of the coupled CFD–DEM method to calculate the particle motion and contact force, the shape of the three-dimensional particle jamming dome and the force chain of clogged particles are investigated. For the first time, we find that the jamming arch that is formed under a higher flow velocity has a larger curvature due to the greater fluid drag acted on the jammed particles.

The rest of paper is organized as follows. Section 2 presents the methodology of the CFD–DEM model. Section 3 introduces the simulation cases used to study the three-dimensional jamming and provides validations of the current simulations. Section 4 shows the simulation results. In this part, the coupled effect of the solid concentration and R on jamming probability are studied. In addition, various ways that the fluid velocity influences jamming at different solid concentrations and different ranges of U_f are systematically investigated. Then, the shape of the jamming dome is discussed and explained based on the force chain figure. Section 5 concludes the paper.

2. Methodology

In the coupled CFD–DEM method, the particle motion is calculated with the DEM approach based on Newton's second law (Cundall and Strack, 1979), and the fluid flow is simulated using the CFD program based on the Navier-Stokes equations (Anderson and Jackson, 1967). The key to the coupling method between CFD and DEM is a proper consideration of the fluid-particle interaction forces (Zhao and Shan, 2013) and the exchange of the interaction forces between the fluid and the particles. In this section, the specific formulas of the particle motion, fluid flow, and fluid-particle interaction force are detailed.

2.1. Mathematical model of particle motion

By employing the DEM method, the particle motions, including translation and rotation, are governed by Newton's second law (Cundall and Strack, 1979):

$$\begin{aligned} m\frac{d\mathbf{u}}{dt} &= \mathbf{f}^{con} + \mathbf{f}^{fp} + m\mathbf{g}, \\ I\frac{d\mathbf{\Psi}}{dt} &= \mathbf{T}^{con}, \end{aligned} \tag{1}$$

ACCEPTED MANUSCRIPT

where, m is the particle mass, $\mathbf{u}$ and $\mathbf{\Psi}$ is the particle's velocity and angular velocity, respectively, and I represents the moment of inertia. $\mathbf{f}^{con}$ is the contact force during particle–particle or particle–wall collision, and $\mathbf{f}^{fp}$ denotes the fluid-particle interaction force. $\mathbf{T}^{con}$ represents the torque due to the particle-particle/wall collision, caused by the tangential contact force, that acted on the contact interface of two particles.(Sun et al., 2007). The normal/tangential contact forces $\mathbf{f}_{n,ij}^{con}/\mathbf{f}_{t,ij}^{con}$ that act on the particle i are as follows (Silbert et al., 2001):

$$\begin{aligned} \mathbf{f}_{n,ij}^{con} &= f(\delta_{ij}/d)(k_n\delta_{ij}\mathbf{n}_{ij} - \gamma_n m_{\text{eff}}\mathbf{V}_{n,ij}), \\ \mathbf{f}_{t,ij}^{con} &= f(\delta_{ij}/d)(-k_t\Delta s_t - \gamma_t m_{\text{eff}}\mathbf{V}_{\mathbf{t,ij}}), \end{aligned} \tag{2}$$

where k_n/k_t are the normal/tangential elastic stiffness constants, and γ_n/γ_t are the normal/tangential viscoelastic damping coefficients for collisions. δ_{ij} is the overlap distance of two particles in contact, namely i and j. $\mathbf{n}_{ij}$ is the unit vector of $\mathbf{r}_{ij}$, which is the direction vector that connects the centres of two particles. $m_{\text{eff}} = m_i m_j/\left(m_i + m_j\right)$ is the effective mass of the spheres with masses m_i and m_j. $\mathbf{V}_{n,ij}$ and $\mathbf{V}_{t,ij}$ are the normal and tangential components, respectively, of the relative velocity of the two particles. Δs_t is the tangential displacement vector between the two spherical particles, which is truncated to satisfy a frictional yield criterion. This yield criterion is characterized by frictional coefficient μ. The tangential force between the two particles grows according to a tangential spring and dash-pot model until $\mathbf{f}_{t,ij}^{con}/\mathbf{f}_{n,ij}^{con} = \mu$ and is then held at $\mathbf{f}_{t,ij}^{con} = \mu\mathbf{f}_{n,ij}^{con}$ until the particles lose contact. When employing the linear Hookean model, the function $f(\delta_{ij}/d)$ is equal to 1.

2.2. Mathematical model for fluid flow

In this work, the fluid flow is solved based on the locally averaged Navier–Stokes equations (Anderson and Jackson, 1967; Xiao and Sun, 2011):

$$\begin{aligned} \nabla\cdot(\phi_s\mathbf{U}_s + \phi_f\mathbf{U}_f) &= 0, \\ \frac{\partial(\phi_f\mathbf{U}_f)}{\partial t} + \nabla\cdot(\phi_f\mathbf{U}_f\mathbf{U}_f) &= \frac{1}{\rho_f}(-\nabla p + \nabla\cdot\tau + \phi_f\rho_f g + \mathbf{F}^{fp}), \end{aligned} \tag{3}$$

where ϕ_s and ϕ_f are the solid and fluid-phase volume fractions of a fluid cell, and $\phi_s + \phi_f = 1$. $\mathbf{U}_s$ and $\mathbf{U}_f$ are the solid- and fluid-phase velocities, respectively. On the right-hand side of the momentum conservation equation, ∇p is the fluid pressure gradient, τ denotes the stress tensor, and $\mathbf{F}^{fp}$ represents the fluid-particle interaction force per unit fluid cell volume V_c, obtained by summing up the fluid forces acting on all the particles in a fluid cell and dividing by V_c (Kafui et al., 2002; Xiao and Sun, 2011):

$$\mathbf{F}_k^{fp} = \sum_{i=1}^{n_{p,k}} \mathbf{f}_i^{fp}/V_{c,k}, \tag{4}$$

with

$$\mathbf{f}_i^{fp} = -V_{p,i}\nabla p + V_{p,i}\nabla\cdot\tau + \mathbf{f}_i^{\prime fp}, \tag{5}$$

ACCEPTED MANUSCRIPT

where k is the cell index, $n_{p,k}$ is the number of the particles in the cell with index k, $\mathbf{f}_i^{fp}$ denotes the fluid–particle interaction acting on the particle with index i. $V_{p,i}$ represents the volume of the particle i. The term $-V_{p,i}\nabla p + V_{p,i}\nabla\cdot\tau$ is due to the macro-scopic variations of the fluid stress, and the component $\mathbf{f'}_i^{fp}$ comes from the detailed variations of the point stress tensor in the fluid flow field around a particle, such as the drag force $\mathbf{f}_i^{drag}$, added mass force $\mathbf{f}_i^{add}$ and lift force $\mathbf{f}_i^{lift}$. Substituting Eq. (5) into Eq. (4) leads to:

$$\mathbf{F}_k^{fp} = -\phi_s\nabla p + \phi_s\nabla\cdot\tau + \sum_{i=1}^{n_{p,k}} \mathbf{f'}_i^{fp}/V_{c,k}. \tag{6}$$

It is noteworthy that the solid volume fraction ϕ_s, solid phase velocity $\mathbf{U}_s$, and fluid-particle interaction force $\mathbf{F}^{fp}$ in Eq. 3 are the Eulerian fields, obtained by implementing a diffusion-based averaging method from discrete particle data (Sun and Xiao, 2015a,b, 2016). This method shows the great robustness and validity to obtain these Eulerian fields, especially when the particle size is closer to or greater than the fluid cell size. The detailed implementation of this method is presented in Appendix A.

2.3. Fluid–particle interactions

In general, the fluid–particle interaction force f_i^{fp} (see Eq. (5)) consists of the pressure gradient force, the drag force, the added mass, and the lift force. Based on our preliminary study of the influence of added mass and lift force on the number of discharged particles N_p, the effect of these two forces on N_p can be neglected. Moreover, the simulation results of N_p without considering these two forces agree well the experimental results of Lafond et al. (2013). Thus, only the drag force and fluid pressure gradient are considered in the fluid–particle interaction force f^{fp} in this work. The formula of the drag force, $\mathbf{f}_i^{drag}$, employed in our simulations is corrected experimentally by considering the hindered settling effect (Syamlal et al., 1993; Sun and Xiao, 2016):

$$\mathbf{f}_i^{drag} = \frac{\pi d_{p,i}^3}{6}\frac{1}{\phi_{f,i}\phi_{s,i}}\beta_i(\mathbf{U}_{p,i} - \mathbf{U}_{f,i}), \tag{7}$$

where $\mathbf{U}_{p,i}$ denotes the velocity of particle i. $\mathbf{U}_{f,i}$, $\phi_{s,i}$, and $\phi_{f,i}$ represents the fluid velocity, the solid volume fraction, and the fluid volume fraction interpolated at the center of particle i, respectively. β_i is the drag correlation which accounts for the presence of other particles.

$$\beta_i = \frac{3}{4}\frac{C_{d,i}}{\mathbf{V}_{r,i}^2}\frac{|\mathbf{U}_{p,i} - \mathbf{U}_{f,i}|}{d_{p,i}}\phi_{f,i}\phi_{s,i}, \text{with} \quad C_{d,i} = (0.63 + 4.8\sqrt{V_{r,i}/\mathrm{Re}_{p,i}})^2, \tag{8}$$

where the particle Reynolds number, $\mathrm{Re}_{p,i}$, is equal to $\rho_f d_{p,i}|\mathbf{U}_{p,i} - \mathbf{U}_{f,i}|/\mu$. $V_{r,i}$ is the ratio of the terminal velocity of a group of particles to the terminal velocity of a single particle.

$$V_{r,i} = 0.5\left(A_{1,i} - 0.06\mathrm{Re}_{p,i} + \sqrt{(0.06\mathrm{Re}_{p,i})^2 + 0.12\mathrm{Re}_{p,i}\,(2A_{2,1} - A_{1,i}) + A_{i,j}^2}\right), \tag{9}$$

with

$$A_{1,i} = \phi_{f,i}^{4.14}$$
$$A_{2,i} = \begin{cases} 0.8\phi_{f,i}^{1.28}, & \text{if} \quad \phi_{f,i} \leq 0.85 \\ \phi_{f,i}^{2.65}, & \text{if} \quad \phi_{f,i} > 0.85 \end{cases} \tag{10}$$

In this work, we use a four-way coupled CFD–DEM solver, *SediFoam*, to simulate the jamming phenomenon. This solver was developed by Xiao and Sun (2011) based on two open-source codes: (a) the CFD toolbox OpenFOAM (OpenCFD, 2013) and (b) the molecular dynamics simulator LAMMPS (Plimpton, 1995). SediFoam has been demonstrated to be a capable tool in simulating many particle flow problems, e.g., a fluidized bed (Xiao and Sun, 2011; Gupta, 2015), sediment transport (Sun and Xiao, 2016), and sedimentation (Xu et al., 2018; Sun et al., 2018), etc. In these areas, the mathematical models mentioned above for the particle motion, fluid flow, and the interaction force have been verified and extensively validated.

3. Implementations and numerical models

3.1. Numerical setup

The geometry of the simulation domain is shown in Fig. 1, in which the x-, y- and z- coordinates represent the length, width, and height directions, respectively. The fluid domain is a square pipe

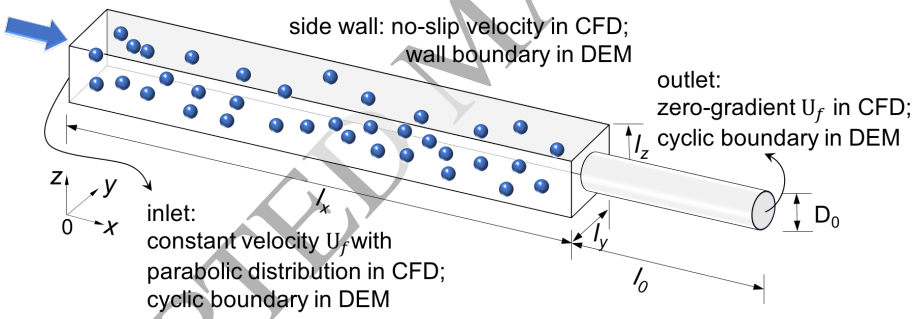

Figure 1: Schematic diagram of the jamming simulation.

connected to a pipe with a smaller diameter. Along the x-direction, the fluid flow enters the domain with a constant velocity from the "inlet" patch and flows out at the "outlet" patch with a zero-gradient velocity. The fluid velocity profile on the "inlet" patch is set as parabolic to ensure that the fluid that enters the pipe is a fully developed laminar flow. Additionally, the "inlet" and "outlet" patches are set as periodic boundaries for the particles in the DEM. As the particles flow out through the "outlet" patch, they enter the simulation domain again from the "inlet" patch. It is noted that when employing the periodic boundary condition, the particles exiting from the "outlet" patch enter the domain with the higher velocity than the fluid velocity on "inlet" patch. To guarantee this entry effect caused by the periodic boundary does not influence the occurrence

ACCEPTED MANUSCRIPT

of jamming, the particles should decelerate to the fluid velocity before entering the constriction. In our simulations, we observed the variation of averaged solid-phase velocity along the flow direction and set the current length of the square pipe longer than the decelerating distance of the particles. Thus, the entry effect of periodic boundary dissipates and does not influence the jamming behavior. In the y- and z- directions, the "wall" boundary is employed for both the fluid and the particles. The other detailed boundary conditions are presented in Fig. 1. The circular pipe starts from $x = 0.05$ m (the location of the orifice) and ends at the "outlet" patch, $x = 0.072$ m. In some previous works on the particle flow, it has been demonstrated that the static particles fixed on the inner surface of a wall could provide a higher effective wall friction than a flat wall (Gupta et al., 2016; Weinhart et al., 2012). For this reason, in the DEM simulation domain, we model the boundary wall of the circular pipe and the patch at the pipe conjunction as the fixed spherical particles, as shown in Fig. 2. It is noteworthy that these added fixed particles are used only to model a flat

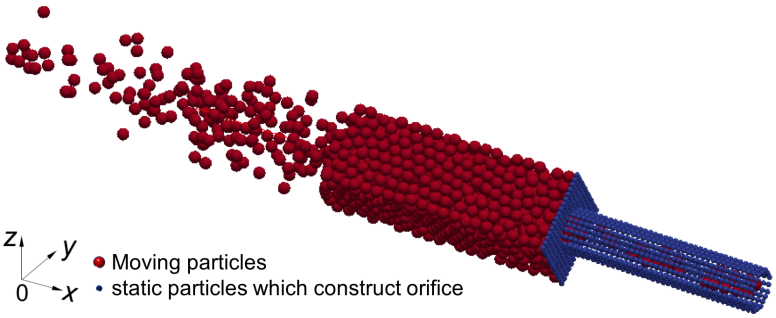

Figure 2: Schematic illustration of fixed and moving particles in simulation domain. The small blue spheres represent the fixed particles that constitute the wall boundary ($d_{pf} = 0.45$ mm), and the large red spheres represent the moving particles.

wall and to restrict the particle motion, which means that they should not have any extra effect on the fluid flow. Thus, the solid concentration and the fluid-particle interaction force of these fixed particles are not considered in the Navier-Stokes equations (Eq. 3). Furthermore, this work aims to study the jamming that occurs in the fluid-driven particle flows. It is the fluid-particle interaction, not the gravity, determining the particle motions and the occurrence of the jamming. Thus, the gravity of the particle and fluid, of which the direction is perpendicular to the flow direction, is not considered here. This neglect corresponds to the physical condition that the particles are neutrally buoyant in the fluid. It is noted that the time spent observing the entire jamming phenomenon $T^*_{observation}$ is defined as four times the journey time $T_{journey}$ that a particle travels from the inlet patch to the orifice, which is equal to l_x/U_f.

There are two series of cases. Case 1 aims to study the coupled effect of solid concentration ϕ_0 and the particle-orifice size ratio R. The particle-orifice size ratio varies from 1.2 to 3.2 by changing the diameter of the moving particles. At different orifice size ratio R, we study the influence of the solid concentration ϕ_0 on jamming probability and find the two characteristic concentrations for

ACCEPTED MANUSCRIPT

Table 1: Parameters of the numerical simulations.

	Case 1 (The coupled effect of $\phi_0 - R$)	Case 2 (The effect of U_f)
Geometry		
width, height, thickness of the square pipe $l_x \times l_y \times l_z$ [mm]	$50 \times 7.2 \times 7.2$	
length, diameter of the circular orifice $l_o \times D_o$ [mm]	22×2.4	
orifice-particle size ratio R	1.2, 1.5, 1.8, 2.0, 2.2, 2.4, 2.8, 3.2	
Mesh resolutions		
width, height, thickness of the square pipe N_{l_x}, N_{l_y}, N_{l_z}	$50 \times 9 \times 9$	
length, diameter of the circular pipe $N_{l_o} \times N_{D_o}$	22×3	
Fluid properties and flow conditions		
kinetic viscosity ν [$\times 10^{-6}$ m^2/s]	1.0	
density ρ_f [$\times 10^3$ kg/m^3]	1.0	
mean flow velocity U_b [m/s]	0.2	0.05, 0.1, 0.15, 0.2, 0.25, 0.3
Reynolds number Re	1440	360, 720, 1080, 1440, 1980, 2160
Particle properties		
fixed particle diameter d_{pf} [mm]	0.45	
moving particle diameter d_{pm} [mm]	0.75, 0.86, 1, 1.09, 1.2, 1.33, 1.6, 2	1
initial solid particle concentration ϕ_0	[0.05–0.60]	[0.05–0.40]
density ρ_s [$\times 10^3$ kg/m^3]	2.65	
stiffness coefficient k_n/k_t [N/m]	5000/1428	
damping coefficient γ_n/γ_t [N/m]	99200/49600	
normal restitution coefficient	0.1	
coefficient of friction	0.4	

ACCEPTED MANUSCRIPT

ACCEPTED MANUSCRIPT

the occurrence of jamming. The initial solid concentration of the particle flow varies from 0.05 to 0.6, with the initial locations of the particles being randomly generated within the entire square pipe. Case 2 aims to investigate the influence of the fluid velocity on jamming. The mean fluid velocity in Case 2 varies from 0.05 m/s to 0.3 m/s (Re = 360 $\sim$ 2160), and the particle velocity is set as the mean fluid velocity of the driven flow. The other parameters of the simulations, including the physical properties of the fluid and particles, are detailed in Tab. 1. It is noted that every simulation case as shown in Tab. 1 is repeated at least ten times, with different random particle seeds, to study the stochastic nature of the jamming problem (Mondal et al., 2016).

3.2. Validation case of the fluid-driven jamming

To validate our model simulating the fluid-driven jamming, we compare the simulation results of fluid pressure drop due to the particle jamming $\Delta P_{jamming}$ with the results obtained by Ergun's equation (Ergun, 1952); and the number of particles discharged before jamming N_p with Lafond's experimental results (Lafond et al., 2013), as shown below. Moreover, the gravity-driven jamming is also simulated to validate the utilization of the fixed particles that construct the orifice, as presented in Appendix B.

3.2.1. Fluid pressure drop caused by the jammed particles

As we know, when fluid flows through a column packed with granular material, the fluid pressure drops due to the kinetic and viscous energy loss (Ergun, 1952). After the particles start to clog the orifice, the particles gradually backlog and form a packed particle column that leads to a fluid pressure drop, $\Delta P_{jamming}$. In our simulations, apart from the pressure drop due to the fluid flows across the abrupt contraction area (orifice), $\Delta P_{orifice}$, the fluid pressure drop, $\Delta P_{jamming}$, caused by jammed particles is observed, as shown in Fig. 3. In addition, accompanying the accumulation of particles, the fluid pressure drop $\Delta P_{jamming}$ increases with the length of the packed particle column. Based on previous works that study the value of $\Delta P_{jamming}$, the widely accepted pressure loss equation was proposed by Ergun (1952) with considering the flow rate, fluid properties, fluid volume fraction, and the parameters of the particle, as shown below:

$$\frac{\Delta P_{jamming}}{L} = 150\frac{(1-\phi_f)^2}{\phi_f^3}\frac{\mu_f U_f}{d_p^2} + 1.75\frac{1-\phi_f}{\phi_f^3}\frac{\rho_f U_f^2}{d_p}, \tag{11}$$

where U_f is the mean velocity of the fluid, μ_f is the dynamic viscosity of the fluid, and L and ϕ_f are the length and the fluid volume concentration of the packed particles, respectively. From our simulations, we obtain the averaged solid concentration of the stable packed particle column and the averaged fluid pressure on the y-z planes along the x-direction when the particles are in a stable jammed state. The fluid volume concentrations of the packed particle column ϕ_f, in our simulations, range from 0.475 to 0.490 (see Fig. 4), which are very close to the value obtained by Mondal et al. (2016), $\phi_f = 0.49$. More importantly, the simulation results of $\Delta P_{jamming}/L$ in different fluid flows are in good agreement with the results calculated by Eq. 11, as shown in Fig. 4.

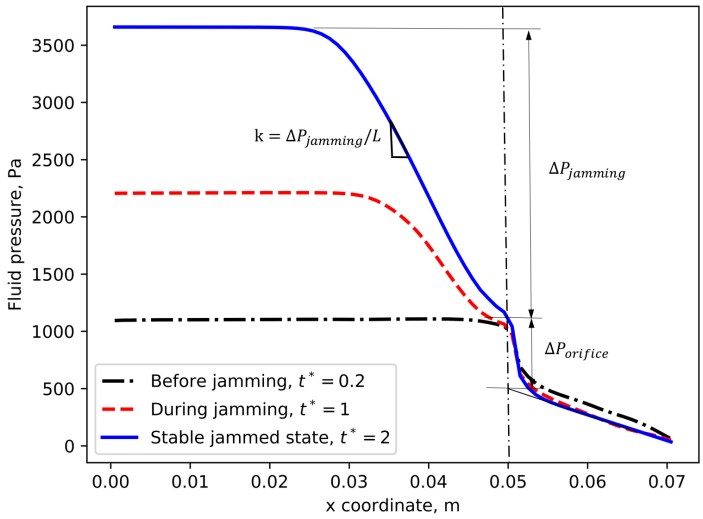

Figure 3: Fluid pressure drop. Case parameters are: $U_f = 0.1$ m/s, $\phi_0 = 0.28$, $d_p = 1$ mm. t^* represents the dimensionless simulation time, defined as $t_{simulation}/T_{journey}$, where $T_{journey}$ is the time of a particle travelling from the inlet patch to the orifice.

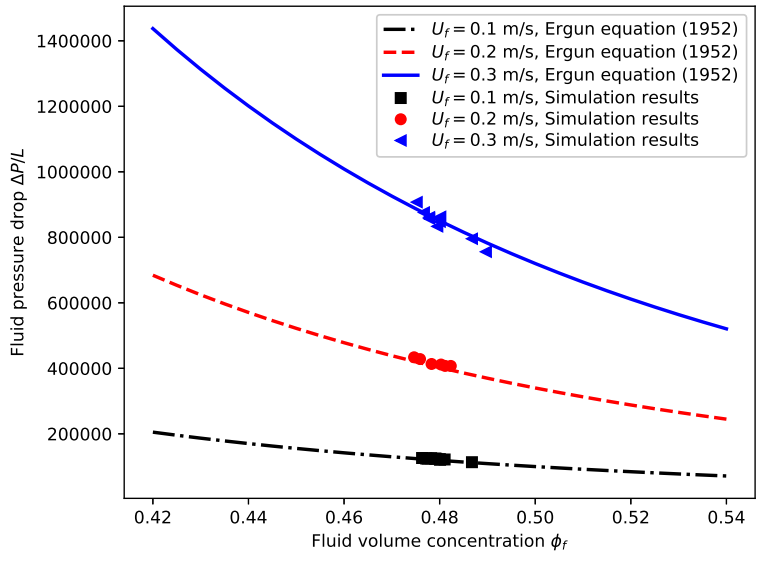

Figure 4: Validation of the pressure loss $\Delta P_{jamming}$ at different fluid velocities. The initial solid volume fraction in these cases is ϕ_0 =0.28, and the orifice-particle size ratio R is 2.4.

The mean mutual deviations of $\Delta P_{jamming}/L$ between the above two methods are 2.73%, 2.47%, and 0.54%, when U_f = 0.1, 0.2, and 0.3 m/s, respectively. This good match of $\Delta P_{jamming}/L$ between our simulation results and the Ergun equation's results validates our numerical models in simulating the particle jammed state at different fluid velocities. Additionally, our simulation model is viable to simulate the jamming that occurs in different fluid velocity flows.

3.2.2. The number of particles discharged before jamming N_p

For the fluid-driven jamming, the number of particles discharged before jamming N_p increases rapidly with the orifice-particle size ratio R. In Lafond's experiments (Lafond et al., 2013) studying the three-dimensional jamming phenomenon, it is found that the logarithm of N_p is linearly dependent on the size ratio R. To validate our simulations, we obtain the N_p and R from simulations and compare them with the experimental results (Lafond et al., 2013). The constriction in

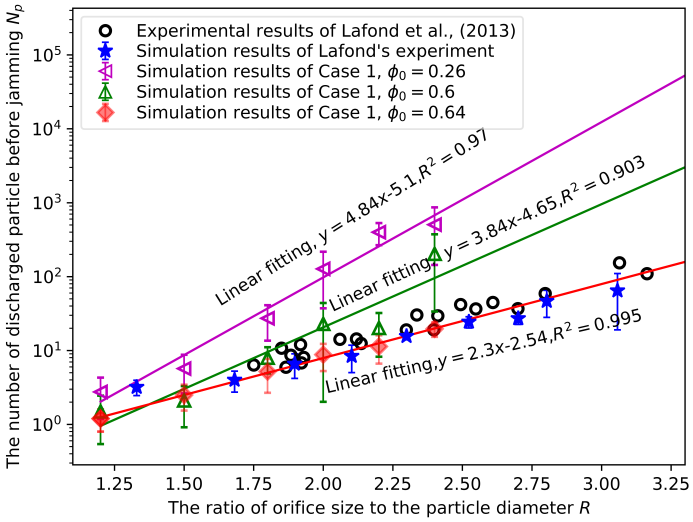

Figure 5: The log-linear relationship between N_p and R. The simulation results of Lafond's experiment are based on the exactly same initial conditions of the experiments "Composition ID: 1-3". The simulations results of Case 1 are fitted by a least squares approach, and the coefficient of determination, also called R-squared, is denoted by R^2.

Lafond's experiments is constructed by the wire mesh, and the long channel flume has the same diameter downstream the constriction. Hence, we firstly run the simulations based on the exactly same initial conditions of his experiments (Composition ID: 1-3), including the particle diameter, the number of particles, and the physical properties of the fluid and particles. As shown in Fig. 5, the simulations results based on the Lafond experiment setup agree very well with the experimental results, which demonstrate the capacity and accuracy of our CFD–DEM simulations. Moreover, we present the results of "Case 1" with different initial solid concentrations in Fig. 5. The log-linear relationship between N_p and R at different solid concentration can be observed. Furthermore, it is

ACCEPTED MANUSCRIPT

found that the slope of the log-linear relationship increases with the rise of solid concentration ϕ_0.

4. Simulation results

4.1. The influence of the particle concentration

4.1.1. The dependence of jamming probability on solid concentration and orifice size ratio

The jamming phenomena have a stochastic nature. Based on previous studies concerning gravity-driven jamming, the jamming probability P_{jam} is mainly controlled by the orifice size ratio R (To et al., 2001; Guariguata et al., 2012). As for the fluid-driven jamming, apart from R, the solid concentration of particle flow ϕ_0 also has a great influence on the jamming probability (Mondal et al., 2016). Hence, the dependence of the jamming probability on solid concentration ϕ_0 and orifice size ratio R is studied in this work, and the simulation results are shown in Fig. 6 (a) and (b). The jamming probability defined here is the number of trials in which jamming occurs divided by the total number of trials (Guariguata et al., 2012). For a better illustration of the effect of the solid concentration on jamming probability, we define the two characteristic initial solid concentrations: $\phi_{threshold}$ and $\phi_{critical}$ to distinguish the jamming state as shown below.

$$P_{jam} = \begin{cases} 0, & \text{when} \quad \phi_0 \leq \phi_{threshold} \\ 0 \sim 1, & \text{when} \quad \phi_0 \in (\phi_{threshold}, \phi_{critical}) \\ 1 & \text{when} \quad \phi_0 \geq \phi_{critical} \end{cases} \tag{12}$$

where $\phi_{threshold}$ represents the threshold solid concentration for the occurrence of jamming. Once $\phi_0 > \phi_{threshold}$, jamming is possible to happen. $\phi_{critical}$ represents the critical concentration for jamming. If $\phi_0 > \phi_{critical}$, jamming definitely occurs. From Fig. 6 (a), the jamming probability increases with the solid concentration ϕ_0 when $\phi_0 \in [\phi_{threshold}, \phi_{critical}]$ at different R. Moreover, as shown in Fig. 6 (b), the jamming probability is determined both by the solid concentration and the orifice-particle size ratio. The value of threshold and critical solid concentration, represented by two white dashed lines in Fig. 6 (b), divide the figure into the three parts: (1). non-jamming zone; (2). definite jamming zone; and (3). uncertain jamming zone. If ϕ_0 and R belong to the non-jamming zone, jamming is unlikely to happen; As ϕ_0 and R are in the "definite jamming zone", the jamming occurs ($P_{jam} = 1$). And when ϕ_0 and R belong to the uncertain jamming zone, P_{jam} increases with ϕ_0 and decreases with R. Furthermore, the values of the threshold and critical concentration $\phi_{threshold}$ and $\phi_{critical}$ increase with the orifice size ratio R, as shown in Fig. 7. This means that the initial solid concentration at which the jamming is possible to occur is higher at the orifice with larger R, which will be explained in Sec. 4.1.2. Notably, it is found that the critical orifice size ratio R_{cr} also exists in fluid-driven jamming. Once the R is larger than R_{cr}, even though the solid particle concentration is very high, the particle jamming does not occur, e.g., when $R = 3.2$, the maximum value of solid concentration $\phi_0 = 0.64$, while $P_{jam} = 0$. Guariguata et al. (2012)

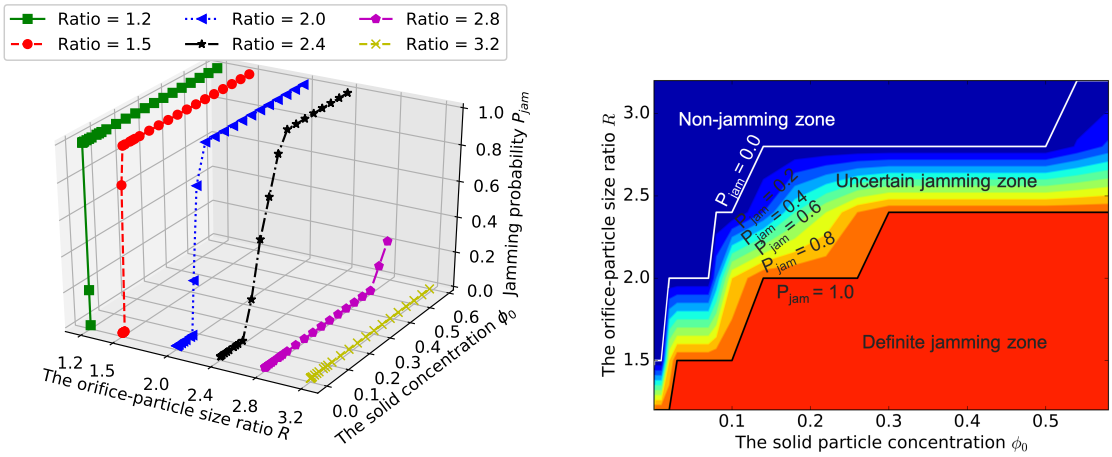

(a) Jamming probability at different ϕ_0 and R (b) Jamming probability contour on the ϕ_0-R plane

Figure 6: Dependence of the jamming probability on solid concentration and orifice size ratio. The fluid velocity U_f is 0.1 m/s.

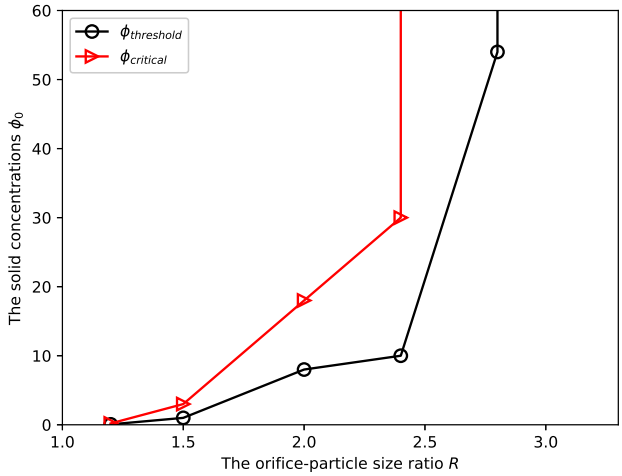

Figure 7: The characteristic solid concentrations $\phi_{threshold}$ and $\phi_{critical}$ versus R

also demonstrated the existence of critical orifice size ratio R_{cr} in the two-dimensional fluid-driven jamming.

4.1.2. The effect of solid concentration on particle discharge properties

The solid concentration ϕ_0 influences not only the jamming probability but also the particle discharge properties, including the particle discharge rate dn/dt on the "outlet" patch and the total number of particles discharged prior to jamming N_p. From our simulations, we find that the variation of particle discharge property can also be distinguished by the characteristic concentrations. Figure 8 illustrates that the value of the discharged particles N_p (represented by the red triangular dot) first increases and then decreases with ϕ_0. N_p reaches to its maximum value at a solid concentration that is close to the critical concentration $\phi_{critical}$. The particle discharge rate dn/dt, which is denoted by the blue circular dot in Fig. 8, also increases with ϕ_0 at a low concentration range. However, when ϕ_0 is greater than a specific concentration that is close to $\phi_{threshold}$, dn/dt does not increase further and remains almost constant with the solid concentration ϕ_0 (see also Fig. 14). This result is attributed to the fact that the orifice has a maximum particle discharge capacity dn/dt_{max} which limits the particle discharge rate dn/dt. When ϕ_0 is greater than $\phi_{threshold}$, the particle discharge rate dn/dt has reached to the value of discharge capacity of the orifice dn/dt_{max}; Although ϕ_0 increases, the dn/dt will keep at the value of dn/dt_{max} and do not increase. In other word, when dn/dt reaches to the maximum discharge capacity of the orifice, it can be inferred the ϕ_0 is greater than $\phi_{threshold}$, and the jamming is possible to occur. Furthermore, it is found that

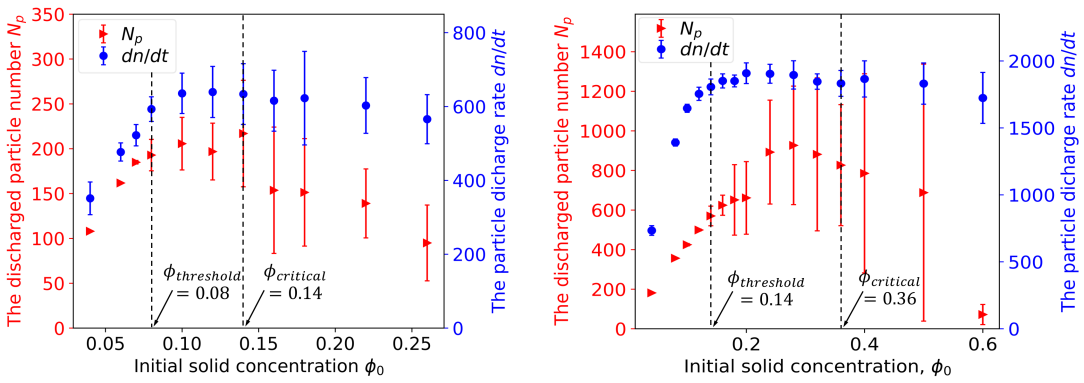

(a) $R = 2$, $U_f = 0.2$ m/s (b) $R = 2.4$, $U_f = 0.2$ m/s

Figure 8: The influence of solid concentration on particle discharge properties. The dots and error bars represent the mean value and standard deviation of quantities of different simulation trials. When ϕ_0 is greater than the $\phi_{threshold}$, the error bars become larger. This is because when jamming does not occur, the particle discharged number and discharge rate is easy to determine with low noise. As the opening size increases, the jamming is possible to happen, the sample standard deviations of N_p and dn/dt rapidly increase because of the stochasticity of the jamming phenomenon.

the maximum discharge capacity of an orifice dn/dt_{max} is dependent on the orifice-particle size ratio R. Lafond et al. (2013) proposed the equation of the maximum discharge rate by substituting the acceleration scales of fluid-driven flow d_p^2/d_p^3 into Beverloo's equation (Beverloo et al., 1961), as shown below:

$$\frac{dn}{dt}_{max} = Cd_p^{-3}(D_o - d_p)^2\sqrt{\frac{d_p^2}{d_p^3}(D_o - d_p)} = C(\frac{D_o}{R})^{-3}(D_o - \frac{D_o}{R})^2\sqrt{(R-1)}, \tag{13}$$

where $C \propto U_f$, which is independent of the particle size and orifice size. Hence, the relevant quantity to collapse the data is $(\frac{D_o}{R})^{-3}(D_o - \frac{D_o}{R})^2\sqrt{(R-1)}$. We obtain the simulation results of dn/dt_{max} at different orifice-particle size ratio R (see Fig. 9 (a)) and plot the relationship between the quantity dn/dt_{max} and $(\frac{D_o}{R})^{-3}(D_o - \frac{D_o}{R})^2\sqrt{(R-1)}$, as shown in Fig. 9 (b). From this figure,

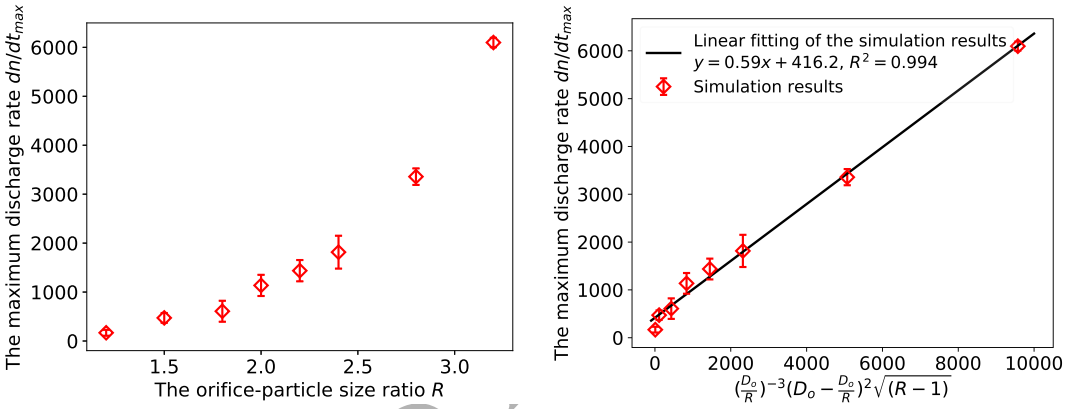

(a) The maximum discharge capacity of an orifice at different orifice-particle size ratio R (b) The discharge capacity dn/dt_{max} vs the quantity $(\frac{D_o}{R})^{-3}(D_o - \frac{D_o}{R})^2\sqrt{(R-1)}$

Figure 9: The simulation results of particle discharge capacity dn/dt_{max} when $\phi_0 = 0.6$, $U_f = 0.2$ m/s.

the linear relationship between dn/dt_{max} and $(\frac{D_o}{R})^{-3}(D_o - \frac{D_o}{R})^2\sqrt{(R-1)}$ proposed by Lafond et al. (2013) can be observed, supporting our analysis of the particle discharge properties. It's shown in Fig. 9 (a) that with the growth of orifice size ratio R, dn/dt_{max} increases significantly. An orifice with a larger size ratio has a greater particle discharge capacity, which can explain why the value of $\phi_{threshold}$ and $\phi_{critical}$ increase with the orifice size ratio R (see Fig. 7). The jamming is possible to occur when $\phi_0 > \phi_{threshold}$, which corresponds to $dn/dt = dn/dt_{max}$. With the increase of R, the orifice's discharge capacity dn/dt_{max} increases. Accordingly, the particle discharge rate dn/dt at $\phi_0 = \phi_{threshold}$ increases, which means the value of $\phi_{threshold}$ rise up. On the other hand, with the decrease of the size ratio R, the value of dn/dt_{max} decreases. The discharge rate dn/dt as jamming occurs becomes lower, and thus $\phi_{threshold}$ decreases.

Apart from P_{jam} and dn/dt, the solid concentration also influences the time T^*_{jam} when jamming occurs. When $\phi_0 > \phi_{critical}$, the time before the particles jam at the orifice decreases with increasing

ϕ_0, as shown in Fig. 10. This change can also be illustrated by the fact that when $\phi_0 > \phi_{critical}$, the number of discharged particles N_p decreases as the solid concentration ϕ_0 increases, while the value of dn/dt remains almost constant (see Fig. 8). Therefore, when $\phi_0 > \phi_{critical}$, T^*_{jam} decreases, and the jamming occurs more quickly at higher solid concentrations.

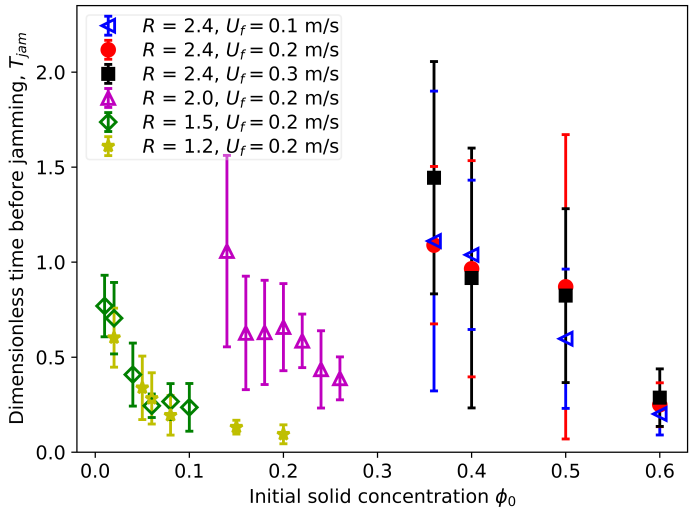

Figure 10: The influence of solid concentration on dimensionless jamming time T^*_{jam}, where $T^*_{jam} = T_{jam}/T_{journey}$.

4.2. The influence of the fluid velocity

For the fluid-driven jamming, the fluid velocity U_f also has an important effect on the jamming probability and the particle discharge property. In this part, the influence of U_f over a range ($0.05 \sim 0.3$ m/s) on jamming is investigated. Firstly, we observe two typical types of jamming in our simulations, referred to as: (a). sequential bridging and (b). multi-particle bridging by Mondal (2013) respectively. Sequential bridging emerges only in low-speed flows with $U_f = 0.05$ m/s and low-solid concentration flow ($\phi_0 < 0.14$), as shown in Fig. 11. During this jamming process, the first particle is stopped on the pipe wall due to the wall friction, and subsequent particles are captured sequentially by the previously deposited particles until the particles clog the pipe and refuse to flow out. The onset of this type of jamming depends on the value of the fluid-driven force acting on the particles. In low-speed and low-solid concentration particle flows, the fluid drag that drives the particles to move is small and can be balanced by the friction force. Thus, the friction force dominates the particles' motion and impedes the particles' motion. This type of jamming can occur anywhere in the pipe of small diameter and does not have the noticeable "jamming dome", as shown in the profile of simulation domain (see Fig. 11). The other type of jamming, called "multi-particle bridging", occurs in the other cases of our simulation. In this type of jamming, many particles flow through the orifice simultaneously. A particle bridge is gradually formed across

the orifice, which results in the jamming phenomenon. The profile of the jamming dome can be observed clearly in Fig. 12.

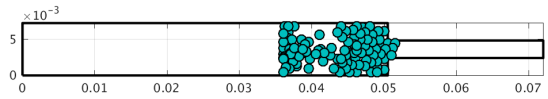

(a) $\phi_0 = 0.08$

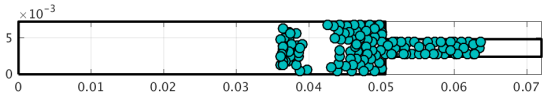

(b) $\phi_0 = 0.10$

Figure 11: Sequential jamming occurs in low-speed and low-solid concentration flows. The fluid velocity $U_f = 0.05$ m/s, orifice-particle size ratio $R = 2.4$.

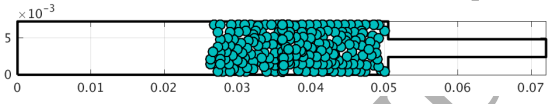

(a) $\phi_0 = 0.28$

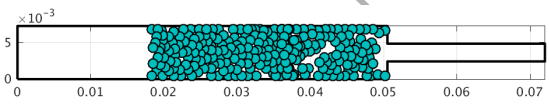

(b) $\phi_0 = 0.40$

Figure 12: Multi-particle bridging. The fluid velocity $U_f = 0.05$ m/s, orifice-particle size ratio $R = 2.4$.

In addition, the fluid velocity U_f influences the jamming probability. According to the previous studies (Mondal et al., 2016), jamming probability P_{jam} increases with the number of particles that pass through the pipe constriction N_p. Before studying the influence of U_f on P_{jam}, we utilize the dimensionless observation time $T^*_{observation}$ to exclude the interference of U_f on N_p. The value of $T^*_{observation}$ is set as four times $T_{journey}$ at different velocity flows ($T_{journey} = 4\frac{l_x}{U_f}$) to allow the same number of particles N_p passing through the constriction. Besides, the initial locations of particles are set as the same at different velocities, so the jamming probability is influenced only by the fluid velocity but not by the initial particle positions. From Fig. 13, when solid concentration ϕ_0 is smaller than 0.14, $P_{jam} = 0.1$ only when $U_f = 0.05$ m/s. This is because "sequential bridging" occurs at the low-concentration and the low-fluid velocity flow. While, when the solid concentration ϕ_0 is greater than 0.14, "multi-particle" bridging occurs. For this type of jamming, the value of P_{jam} at $U_f = 0.3$ m/s is the maximum, and the P_{jam} at $U_f = 0.05$ m/s is minimum. With the increase of the fluid velocity, the jamming probability P_{jam} increases, especially when $U_f < 0.2$ m/s. However, there is a singularity at $\phi_0 = 0.18$, where P_{jam} at $U_f = 0.2$ m/s is smaller than that at $U_f = 0.1$ m/s. This may come from the stochastic property of the jamming. Dai and

Grace (2010) proposed that the reason why P_{jam} increases with the U_f is that more particles pass through the orifice simultaneously at the higher U_f. Hence, we obtain the particle discharge rate dn/dt at different fluid velocities.

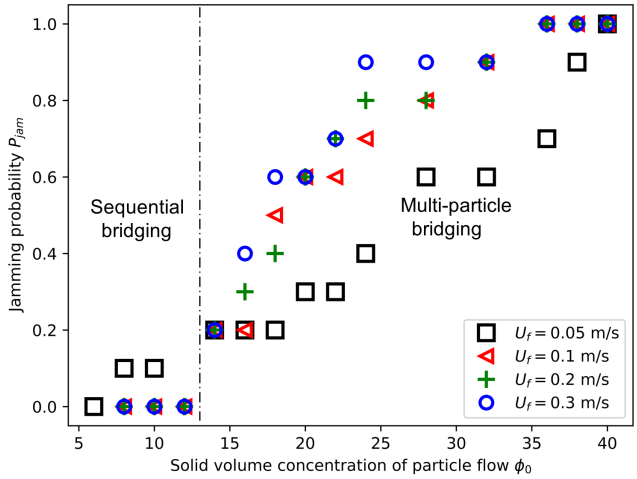

Figure 13: Dependence of jamming probability on the solid concentration ϕ_0 and the fluid velocity U_f. The orifice-particle size ratio R is 2.4.

As is shown in Fig. 14, when $\phi_0 > \phi_{threshold}$, the particle discharge rate dn/dt reaches to the maximum value dn/dt_{max}, and the jamming is possible to happen ($P_{jam} > 0$). More importantly, the value of maximum discharge rate dn/dt_{max} is greater at the higher fluid velocity; Accordingly, the value of P_{jam} is higher (see Fig. 13). It has been demonstrated the N_p is not the reason that P_{jam} increases with the increase of the U_f. From Fig. 13 and Fig. 14, the reason that the P_{jam} increases with U_f is that dn/dt_{max} increases with U_f. In the flow with the higher velocity, more particles are passing through the orifice per unit time, hence the jamming probability increases. Furthermore, we acquire the dn/dt_{max} over a wide range of the fluid velocity to discuss the dn/dt_{max}–U_f relationship, as shown in Fig. 15. We find that the dn/dt_{max}–U_f correlation is different at different range of fluid velocity. When U_f is lower than 0.15 m/s, the value of dn/dt_{max} is proportional to the U_f, which is the same as the assumption $C \propto U_f$ in Eq. 13 proposed by Lafond et al. (2013). However, when U_f is high, the slope of the dn/dt_{max}–U_f correlation decreases. And when U_f is higher than 0.25 m/s, dn/dt_{max}–U_f lines become almost flat. The low-gradient part of dn/dt_{max}–U_f relationship indicates that the fluid velocity has the relatively small effect on the maximum particle discharge rate dn/dt_{max} when U_f is high. Since the P_{jam} is related to the dn/dt_{max}, the effect of U_f on dn/dt_{max} also can be presented on the effect of U_f on P_{jam}. For example, at $R = 2.4$, when $U_f > 0.2$ m/s, dn/dt_{max} increases slightly with the U_f; Accordingly, the jamming probability does not increase significantly with the fluid velocity (see Fig. 13). Guariguata

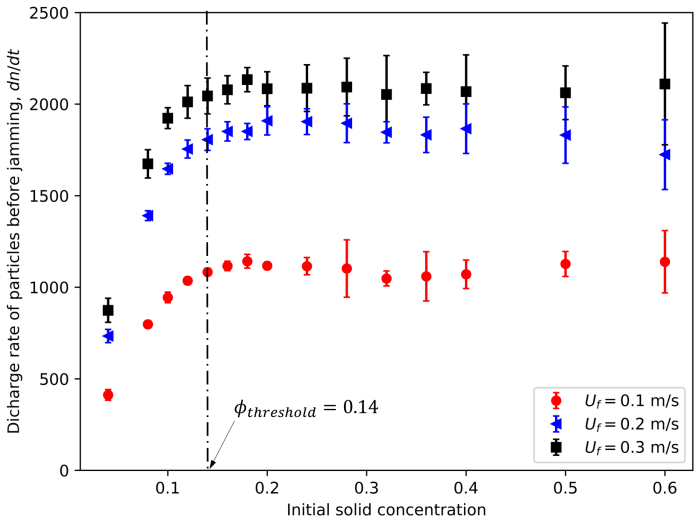

Figure 14: The maximum discharge rate of particles under different fluid velocities. The orifice-particle size ratio in these cases is 2.4.

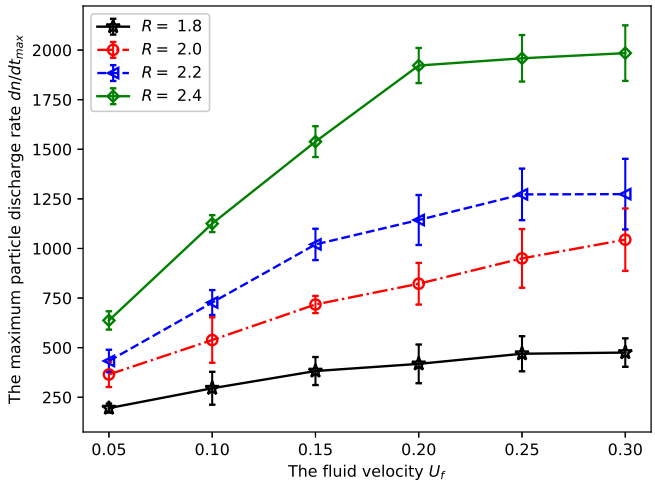

Figure 15: The simulation results of particle discharge rate at different fluid velocities.

et al. (2012) also did not observe the apparent influence of the fluid velocity U_f on the jamming probability P_{jam}. This may attribute that the fluid velocity U_f in his experiments is relatively high ($U_f = 0.14 \sim 0.3$ m/s), which has the insignificant effect on dn/dt. Therefore, in this small range of fluid velocity, the variation of P_{jam} with U_f is invisible.

4.3. Jamming dome

For the "multi-particle bridging" case, a three-dimensional jamming dome forms at the orifice. We can track every particle's motion, location and the contact force from the DEM simulations. Therefore, the shape of the jamming dome and the factors that contribute to it are first investigated here. Because of the rotational symmetry of the three-dimensional dome, we plot the two-dimensional profile of it for a direct and visualized observation. As is shown in Fig. 16, the jammed particles of which the z-coordinate $\in$ (0.00355,0.00365) m are presented by the hollow circles, which forms an obvious jamming arch near the orifice. In this work, we consider the jamming

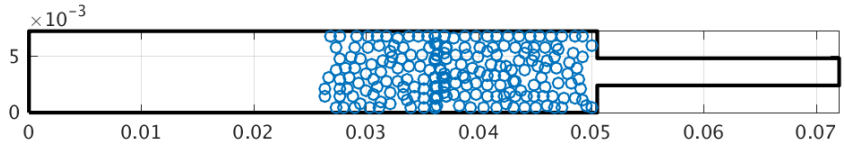

(a) $U_f = 0.05$ m/s

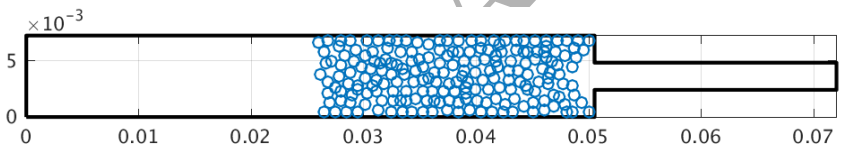

(b) $U_f = 0.1$ m/s

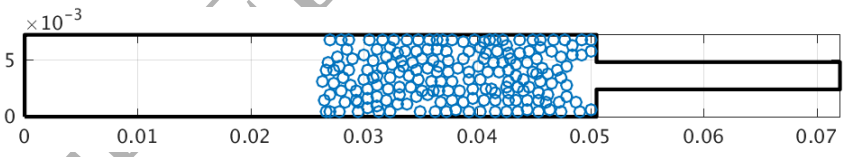

(c) $U_f = 0.2$ m/s

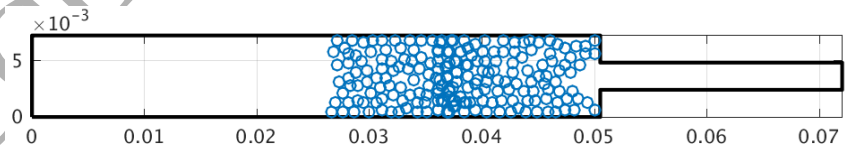

(d) $U_f = 0.3$ m/s

Figure 16: Middle cross-section of the three-dimensional jamming dome. The initial solid volume $\phi_0 = 0.28$, and the orifice-particle size ratio $R = 2.4$.

arch as the most common parabolic arch (Vaidyanathan and Perumal, 2004) and fit the locations of

the bridged particles with a parabolic function, $x = Ay^2 + By + C$, where x and y here represent the x- and y- coordinate of the particle location; And A represents the curvature of the arch. Figure 17 shows that the curvature of the arch A increases with fluid velocity U_f, which means the jamming arch formed in the higher-speed particle flow bends more sharply.

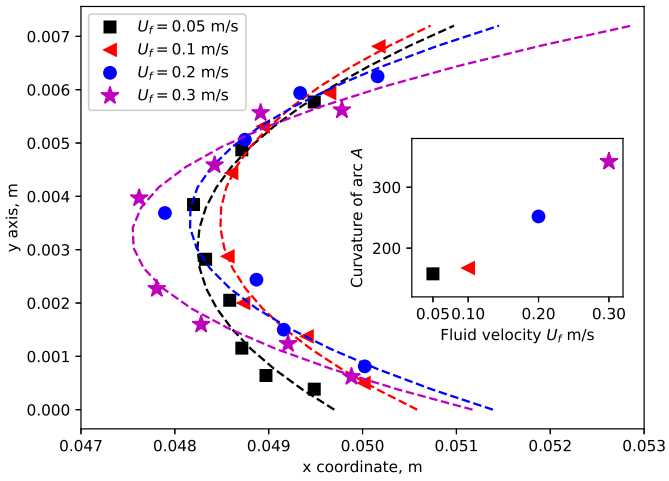

Figure 17: The parabolic jamming arch. The initial solid volume $\phi_0 = 0.28$, and the orifice-particle size ratio $R = 2.4$.

We infer that the influence of the fluid velocity on the shape of the arch is due to different fluid drag exerted on the jammed particles. With increasing the fluid velocity U_f, the fluid drag acting on the clogged particles rises, and the inter-particle contact force grows. From our simulation, the value of the inter-particle contact force can be presented by the force chain figure of the particles, as is shown in Fig. 18. The value of the inter-particle contact force is larger in the higher-speed flow, represented by the larger-diameter cylinder with the darker colour. Moreover, we calculate the value of averaged contact stress σ^{con} on the y-z planes proposed by Xu et al. (2018), which increases obviously with the fluid velocity, as shown in Fig. 19. The value of contact force between particles, whether in the bulk of the packed column or in the jamming arch, is both greater in the higher-speed flow due to the greater fluid drag force. The drastic increase of contact stress at $x = 0.0475 \sim 0.0485$ m is attributed to the existence of the jamming arch, which decreases the effective contacted area of packed particles.

Furthermore, the force acting on the particles influences the shape of the jamming dome. The particle jamming dome can be stable only when the tangential contact force satisfies the frictional yield criterion $\sigma_t^{con} <= \mu\sigma_n^{con}$. The dome with a larger curvature can resolve more fluid drag into a normal direction, and, in turn, eliminate the tangential contact force. Thus, the jamming dome with a larger curvature can bear a greater fluid drag and remain stable in a higher-speed flow. In contrast, if the jamming dome has the small curvature, the tangential contact force resolved from

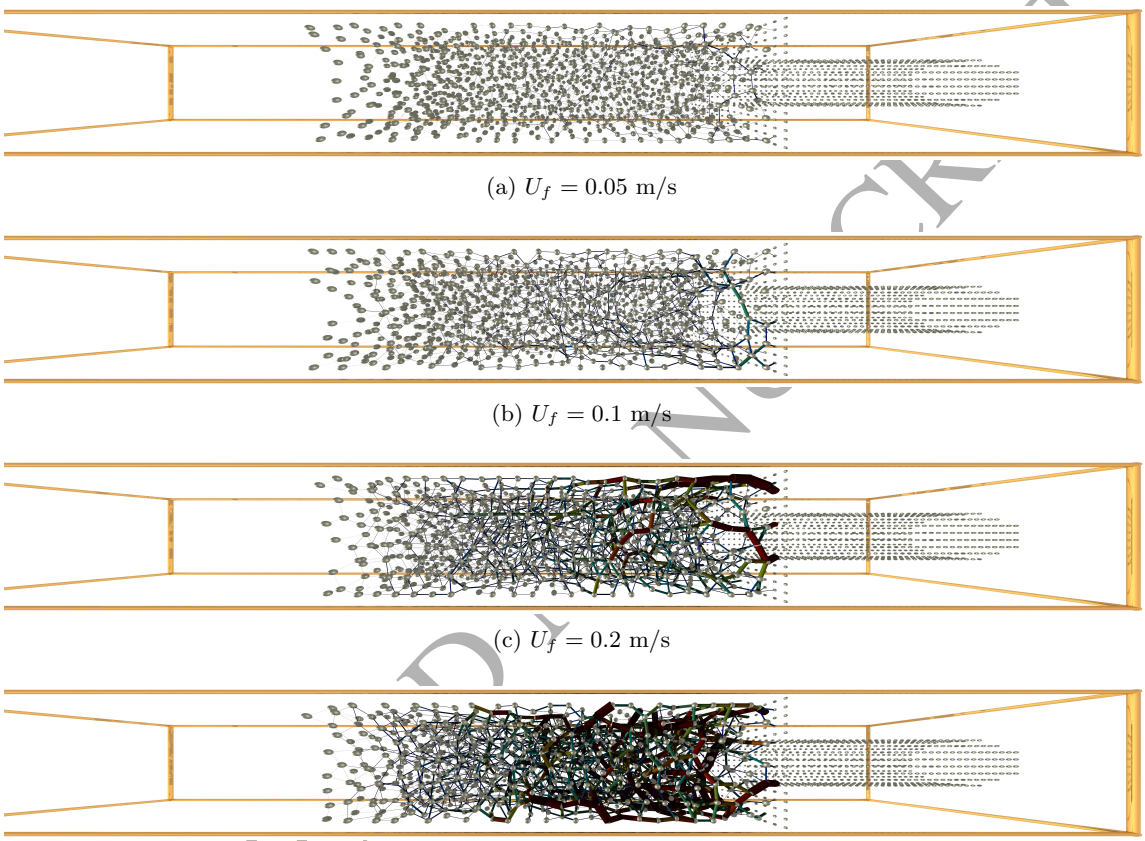

(a) $U_f = 0.05$ m/s

(b) $U_f = 0.1$ m/s

(c) $U_f = 0.2$ m/s

(d) $U_f = 0.3$ m/s

Figure 18: Force chain among particles obtained at different fluid velocity when $\phi_0 = 0.28$, $R = 2.4$. The spheres represent the particles, of which the sizes are scaled by a factor of 0.15. The diameters and the colour of the cylinders indicate the value of contact force among particles.

the fluid drag is larger and cannot be balanced by the maximum frictional force, and thus, the jamming arch with a small curvature can not form in the high-speed flow. In summary, with the increase of the fluid velocity, the curvature of the jamming arch increases.

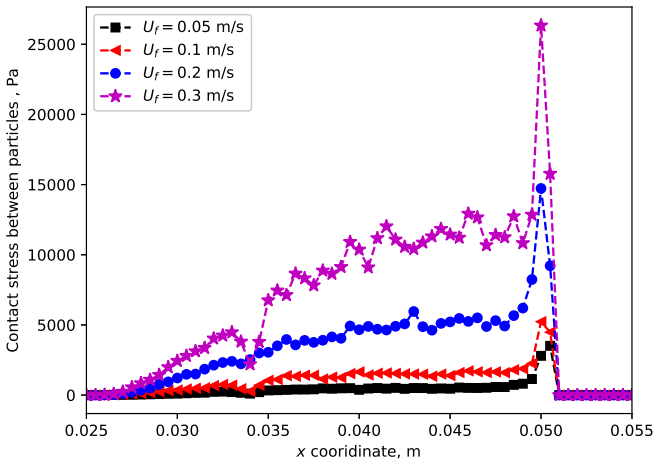

Figure 19: The averaged contact stress σ_{con} between particles along the x-direction when $\phi_0 = 0.28$ and $R = 2.4$.

5. Conclusion

By employing the coupled CFD–DEM, this work investigates the three-dimensional fluid-driven jamming phenomenon. The simulation model is firstly validated by the N_p–R relationship and the pressure loss $\Delta P_{jamming}$. The close match between our simulation results and the results of previous works demonstrates the validity and capacity of the current model. Then, we discuss three critical factors that influence the occurrence of the fluid-driven jamming, i.e., the orifice-particle size ratio R, the initial solid concentration ϕ_0, and the fluid velocity U_f. The concluding effects of these factors are detailed as follows:

1. When the initial solid concentration ϕ_0 is greater than $\phi_{threshold}$, the jamming is possible to occur, and the jamming probability increases with the ϕ_0. Once the ϕ_0 is greater than $\phi_{critical}$, the jamming definitely occurs ($P = 1$). Furthermore, the occurrence of jamming is related to the particle discharge rate dn/dt. When dn/dt reaches to the maximum discharge capacity of the orifice dn/dt_{max}, the jamming is possible to happen ($P > 0$). In addition, the time when jamming occurs is influenced by the solid concentration ϕ_0. When $\phi_0 \geq \phi_{critical}$, jamming occurs more quickly in the higher solid concentration flow.
2. The coupled effect of the solid concentration and the orifice size ratio on jamming probability is also studied here. It is found that with the increase of the orifice size, the value of $\phi_{threshold}$ and $\phi_{critical}$ increases. This is because the maximum discharge capacity of the orifice dn/dt_{max}

ACCEPTED MANUSCRIPT

increases with the orifice size ratio R. An orifice with a larger size ratio has a greater discharge capacity that allows more particles to flow through. Therefore, the maximum value of the particle discharge rate dn/dt is higher, and accordingly the value of $\phi_{threshold}$ is higher. For an orifice with a larger size ratio R, jamming is possible to happen in the higher solid concentration flow. However, there is a critical orifice size ratio at which the jamming is impossible to happen even if ϕ_0 is very high.

3. The influence of the fluid velocity on jamming is complex and varies with the solid concentration and the fluid velocity. It is found that U_f influences the type of jamming, the jamming probability, and the shape of the jamming dome. The sequential jamming without a jamming dome occurs in the particle flow with the low solid concentration and the low speed. Otherwise, the multi-particle bridging occurs. For the multi-particle bridging, the jamming probability increases with the fluid velocity due to the increase of the maximum particle discharge rate dn/dt_{max}. However, when the fluid velocity is high, the effect of the fluid velocity on jamming probability becomes insignificant because the dn/dt_{max} is not significantly influenced by the fluid velocity. Additionally, the fluid velocity has the effect on the shape of the jamming dome. With the increase of the fluid velocity, the fluid drag exerted on the clogged particles increases, and thus the curvature of the jamming arch grows.

Acknowledgements

This work is supported by the State Scholarship Fund of China scholarship council, the National Key R&D Program of China (Grant No. 2016YFC0800200), the Projects of International Cooperation and Exchanges NSFC (Grant No. 51620105008), the National Science Foundation for Young Scientists of China (Grant No. 51608482) and the National Natural Science Foundation of China (Grant No. 51478424).

References

References

Anderson, T., Jackson, R., 1967. A fluid mechanical description of fluidized beds: Equations of motion. Industrial and Chemistry Engineering Fundamentals 6, 527–534.

Beverloo, W. A., Leniger, H. A., Van de Velde, J., 1961. The flow of granular solids through orifices. Chemical engineering science 15 (3-4), 260–269.

Cundall, P., Strack, D., 1979. A discrete numerical model for granular assemblies. Géotechnique 29, 47–65.

Dai, J., Grace, J. R., 2010. Blockage of constrictions by particles in fluid–solid transport. International Journal of Multiphase Flow 36 (1), 78–87.

ACCEPTED MANUSCRIPT

Ergun, S., 1952. Fluid flow through packed columns. Chem. Eng. Prog. 48, 89–94.

Guariguata, A., Pascall, M. A., Gilmer, M. W., Sum, A. K., Sloan, E. D., Koh, C. A., Wu, D. T., 2012. Jamming of particles in a two-dimensional fluid-driven flow. Physical Review E 86 (6), 061311.

Gupta, P., 2015. Verification and validation of a DEM–CFD model and multiscale modelling of cohesive fluidization regimes.

Gupta, P., Sun, J., Ooi, J., 2016. DEM-CFD simulation of a dense fluidized bed: Wall boundary and particle size effects. Powder Technology 293, 37–47.

Hilton, J., Cleary, P., 2011. Granular flow during hopper discharge. Physical Review E 84 (1), 011307.

Janda, A., Zuriguel, I., Maza, D., 2012. Flow rate of particles through apertures obtained from self-similar density and velocity profiles. Physical review letters 108 (24), 248001.

Kafui, K., Thornton, C., Adams, M., 2002. Discrete particle-continuum fluid modelling of gas–solid fluidised beds. Chemical Engineering Science 57 (13), 2395–2410.

Lafond, P. G., Gilmer, M. W., Koh, C. A., Sloan, E. D., Wu, D. T., Sum, A. K., 2013. Orifice jamming of fluid-driven granular flow. Physical Review E 87 (4), 042204.

Liu, A. J., Nagel, S. R., 1998. Nonlinear dynamics: Jamming is not just cool any more. Nature 396 (6706), 21.

Mondal, S., 2013. Flow of particulate suspensions through constrictions: multi-particle effects.

Mondal, S., Wu, C.-H., Sharma, M. M., 2016. Coupled CFD–DEM simulation of hydrodynamic bridging at constrictions. International Journal of Multiphase Flow 84, 245–263.

OpenCFD, 2013. OpenFOAM User Guide. See also `http://www.opencfd.co.uk/openfoam`.

Plimpton, J., 1995. Fast parallel algorithms for short-range molecular dynamics. J. Comp. Phys. 117, 1–19, see also `http://lammps.sandia.gov/index.html`.

Silbert, L. E., Ertaş, D., Grest, G. S., Halsey, T. C., Levine, D., Plimpton, S. J., 2001. Granular flow down an inclined plane: Bagnold scaling and rheology. Physical Review E 64 (5), 051302.

Sun, J., Battaglia, F., Subramaniam, S., 2007. Hybrid two-fluid DEM simulation of gas-solid fluidized beds. Journal of Fluids Engineering 129 (11), 1394–1403.

Sun, R., Xiao, H., 2015a. Diffusion-based coarse graining in hybrid continuum–discrete solvers: Applications in CFD–DEM. International Journal of Multiphase Flow 72, 233–247.

ACCEPTED MANUSCRIPT

Sun, R., Xiao, H., 2015b. Diffusion-based coarse graining in hybrid continuumdiscrete solvers: Theoretical formulation and a priori tests. International Journal of Multiphase Flow 77, 142 – 157.

Sun, R., Xiao, H., 2016. SediFoam: A general-purpose, open-source CFD–DEM solver for particle-laden flow with emphasis on sediment transport. Computers & Geosciences 89, 207 – 219.

Sun, R., Xiao, H., Sun, H., 2018. Investigating the settling dynamics of cohesive silt particles with particle-resolving simulations. Advances in Water Resources 111, 406–422.

Syamlal, M., Rogers, W., O'Brien, T., 1993. MFIX documentation: Theory guide. Tech. rep., National Energy Technology Laboratory, Department of Energy, see also URL `http://www.mfix.org`.

To, K., Lai, P.-Y., Pak, H., 2001. Jamming of granular flow in a two-dimensional hopper. Physical review letters 86 (1), 71.

Vaidyanathan, R., Perumal, P., 2004. Structural Analysis Vol II. Vol. 2. Laxmi Publications.

Weinhart, T., Thornton, A. R., Luding, S., Bokhove, O., 2012. Closure relations for shallow granular flows from particle simulations. Granular Matter 14 (4), 531–552.

Xiao, H., Sun, J., 2011. Algorithms in a robust hybrid CFD–DEM solver for particle-laden flows. Communications in Computational Physics 9 (2), 297–323.

Xu, S.-l., Sun, R., Cai, Y.-q., Sun, H.-l., 2018. Study of sedimentation of non-cohesive particles via CFD–DEM simulations. Granular Matter 20 (1), 4.

Zhao, J., Shan, T., 2013. Coupled CFD–DEM simulation of fluid–particle interaction in geomechanics. Powder technology 239, 248–258.

Zhu, H., Zhou, Z., Yang, R., Yu, A., 2007. Discrete particle simulation of particulate systems: theoretical developments. Chemical Engineering Science 62 (13), 3378–3396.

Zuriguel, I., Garcimartín, A., Maza, D., Pugnaloni, L. A., Pastor, J., 2005. Jamming during the discharge of granular matter from a silo. Physical Review E 71 (5), 051303.

Appendix A. Diffusion-based averaging method

The solid volume fraction ϕ_s, solid phase velocity $\mathbf{U}_s$, and fluid-particle interaction force $\mathbf{F}^{fp}$ is obtained by implementing a robust diffusion-based averaging method from discrete particle data

ACCEPTED MANUSCRIPT

(Sun and Xiao, 2015a,b, 2016). The first step of this method is averaging these fields, e.g. the solid volume fraction ϕ_s, based on the particle centroid method (PCM):

$$\phi_{s,k} = \frac{\sum_{i=1}^{n_{p,k}} V_{p,i}}{V_{c,k}}, \tag{A.1}$$

where k is the fluid cell index. $\phi_{s,k}$ is the solid volume fraction of cell k and $V_{c,k}$ is the volume of cell k. $n_{p,k}$ denotes the number of particles in fluid cell k, $V_{p,i}$ is the volume of particle i. The obtained $\phi_{s,k}$ by using PCM method is served as the initial condition $\phi_{s,k}|_{t=0}$ for the following diffusion equation (Sun and Xiao, 2015a,b):

$$\frac{\partial \phi_s}{\partial \tau} = \nabla^2 \phi_s \qquad \text{for} \quad \mathbf{x} \in \Re^3, \tau > 0, \tag{A.2}$$

where $\mathbf{x}$ is spatial coordinate; $\nabla^2\phi_s = \partial^2\phi_s/\partial x^2 + \partial^2\phi_s/\partial y^2 + \partial^2\phi_s/\partial z^2$. Integrating the above diffusion equations (Eq. A.2) with the initial conditions (Eq. A.1) and zero-gradient condition at the physical boundary until time $\tau = T$, the obtained $\phi_s(\mathbf{x}, T)$ is the averaged field to be used in our simulations. The similar diffusion based coarse graining method is implemented to acquire $\mathbf{U}_s$ and $\mathbf{F}^{fp}$ in Eq. 3. It is noteworthy that $\mathbf{U}_s$ and $\mathbf{F}^{fp}$ is not calculated directly, while the quantities $\phi_s\mathbf{U}_s$, and $\phi_f\mathbf{Fm}^{fp}$ are chosen to solve in the diffusion equations due to the conservation requirements, i.e.,

$$\text{particle momentum: } \rho_s \sum_{k=1}^{N_c} \phi_{s,k} V_{c,k} \mathbf{U}_{s,k} = \sum_{i=1}^{N_p} \rho_s V_{p,i} \mathbf{U}_{p,i} \tag{A.3}$$

$$\text{fluid–particle interaction force: } \sum_{k=1}^{N_c} (1-\phi_{s,k}) \rho_f V_{c,k} \mathbf{Fm}_k^{fp} = \sum_{i=1}^{N_p} \mathbf{f}_i^{fp} \tag{A.4}$$

where N_c and N_p represents the total number of fluid cells and particles in system. $\mathbf{U}_{s,k}$ is the Eulerian solid phase velocity in cell k, and $\mathbf{Fm}_k^{fp}$ denotes the fluid-particle interaction force per unit fluid mass in cell k. Finally, divide the diffusion-based averaged quantity $\phi_s\mathbf{U}_s(\mathbf{x}, T)$ by $\phi_s(\mathbf{x}, T)$, and multiply the quantity $\phi_f\mathbf{Fm}^{fp_k}(\mathbf{x}, T)$ by ρ_f, to obtain $\mathbf{U}_s$ and $\mathbf{F}^{fp}$, respectively. This method has been demonstrated to be equivalent to the statistical kernel method with a Gaussian kernel (i.e., the bandwidth of Gaussian kernel $b = \sqrt{4T}$) (Sun and Xiao, 2015a,b) but is more convenient to implement in CFD–DEM simulations.

Appendix B. Validation case of the gravity-driven jamming

Before validating the fluid-driven jamming cases, we first performed a simulation of gravity-driven jamming to validate our DEM model. Same as Zuriguel's experimental setup (Zuriguel et al., 2005), a cylindrical silo has the diameter of 30 cm. The flat base of the silo with a circular hole is also modeled by the fixed particles. Besides, the particle properties are based on the "Set

1" experiment of Zuriguel et al. (2005), where $d_p = 0.001$ m and $\rho_p = 2200\ kg/m^3$. In place of the jet of pressurized air from beneath the orifice that triggered the avalanche in the experiments, we utilized a frictional wall to accumulate the packed particles and then unfixed the wall to release the particles. As proposed by Zuriguel et al. (2005), when the orifice-particle size ratio R is smaller

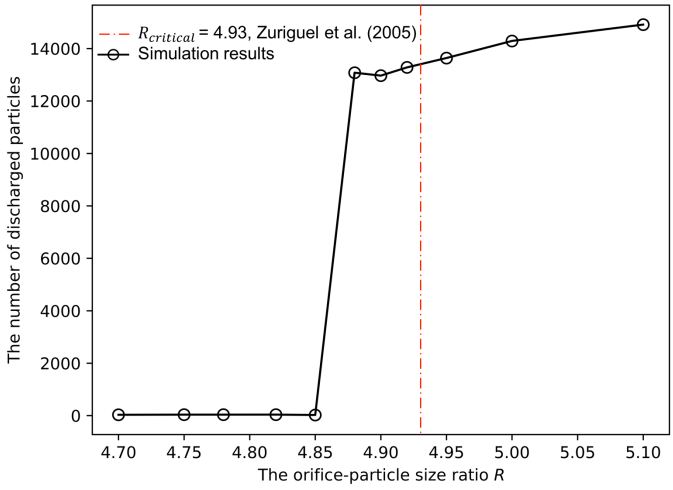

Figure B.20: The number of discharged particles at different R

than a critical size ratio R_{cr}, the particles clog the silo's outlet, and the particle jamming occurs. On the otherwise, once the orifice-particle size ratio exceeds the critical size ratio, the particles fall continuously from the silo without jamming. In our simulations, we found that when orifice-particle size ratio R is smaller than 4.85, the particle jamming occurs. The number of discharged particles is very small, which is in the range of [24, 38] when $R \in [4.70, 4.85]$. However, when $R >= 4.88$, the particles fall continuously without jamming, the number of discharged particles increases sharply from 24 ($R = 4.85$) to 13078 ($R = 4.88$), as shown in Fig. B.20. This means that the critical size ratio obtained in our simulation is in the range of [4.85, 4.88], which is very close to the value of R_{cr}, 4.94 ± 0.03, obtained in Zuriguel's experiment (2005). This close agreement validates our model for simulating the gravity-driven jamming and demonstrates the validity of the utilization of the fixed particles that constructs the hole/orifice.

ACCEPTED MANUSCRIPT